Quantifying Fano properties in self-assembled metamaterials

Radius N. S. Suryadharma*
Institute of Theoretical Solid State Physics, Karlsruhe Institute of Technology, Wolfgang-Gaede-Strasse 1, 76131 Karlsruhe, Germany

Carsten Rockstuhl
Institute of Theoretical Solid State Physics, Karlsruhe Institute of Technology, Wolfgang-Gaede-Strasse 1, 76131 Karlsruhe, Germany and Institute of Nanotechnology, Karlsruhe Institute of Technology, P.O. Box 3640, 76021 Karlsruhe, Germany

Olivier J. F. Martin
Nanophotonics and Metrology Laboratory (NAM), Swiss Federal Institute of Technology Lausanne (EPFL), 1015, Lausanne, Switzerland

Ivan Fernandez-Corbaton
Institute of Nanotechnology, Karlsruhe Institute of Technology, P.O. Box 3640, 76021 Karlsruhe, Germany

(Received 4 April 2019; revised manuscript received 23 April 2019; published 10 May 2019)

Fano resonances in metamaterials can be explained by the coupling between different modes sustained by the meta-atom. While the associated spectral features are usually quite easy to identify for top-down metamaterials, thanks to the deterministic arrangement of the meta-atom relative to the illumination, the identification of spectral features due to Fano resonances is much more challenging for bottom-up metamaterials. There, the response is spurred by the random arrangement of the meta-atoms relative to the illumination. To improve the situation, we introduce a quantity that measures the nonorthogonality of the modes sustained by the meta-atom. The measure allows us to disclose whether specific details in the spectral response emerge from Fano features or whether they are only due to the incoherent superposition of different modes. We strengthen our argumentation while discussing the multipolar decomposition of the different modes that contribute to the Fano features for a representative meta-atom.

DOI: 10.1103/PhysRevB.99.195416

I. INTRODUCTION

Fano resonances attract attention due to their sharp spectral features [1–3]. In the field of metamaterials, a Fano resonance arises because of an intricate scattering response from the basic building block, the so-called meta-atom [4]. Multiple applications have been suggested to exploit Fano resonances. Prime examples are optical switches [5] or optical sensing devices [6,7]. Besides, the anomalous properties of Fano resonances in the near field of the scatterer can also be used for surface-enhanced Raman scattering [8,9] to enhance the nonlinear response [10,11] or to enhance circular dichroism [12,13].

The origin of a Fano resonance is frequently explained in terms of spectral interference between modes sustained by the meta-atom [1,2]. For a particular incident field, a few or at least two modes supported by the structure have to be excited simultaneously. If the excited modes are mutually nonorthogonal, a cross coupling occurs that manifests in constructive or destructive interference of spectrally observable quantities. Frequently, one of the modes is assumed to be spectrally broad, showing a weak dispersion in its spectral phase. It is called the bright mode. The other mode is usually assumed to be spectrally narrow, giving rise to a rather strong dispersion in its spectral phase. The mode is frequently called dark as the sharp spectral features can arise from suppressing radiative losses. The interference between the modes results in sharp spectral features in the overall optical response. A prototypical system whose response can be fully captured by such line of argument is the dolmen structure [14,15].

For a structure consisting of many particles, however, it is challenging to identify the involved modes. It is complicated because the properties of these assemblies cannot be explained in terms of modes supported by each constituent but rather as supermodes of interacting particles [16]. These supermodes depend on the arrangement of the particles and their geometry. For this reason, the consideration of collective eigenmodes of the entire structure as opposed to the interaction of eigenmodes of the isolated subsystem has been used to explain Fano features [17–19]. Since this approach relies on modes supported by the structure, their identification is of utmost importance to understand the emergence of the Fano features.

The identification of the modes requires the discussion of the properties of the scatterer in the absence of an illumination. This is challenging, as the scatterer constitutes an open system and the corresponding operator is non-Hermitian [20]. Several approaches have been developed to extract modes from the relevant scattering operator. The singular expansion method from the integral operator [21,22], the characteristic mode approach using an impedance matrix obtained from the

*radius.suryadharma@kit.edu

method of moments [23,24], eigenmode analysis from volumetric method of moments [25,26], inverse scattering matrix using Fourier modal method [27], poles in complex frequency plane of the scattering matrix [28], and the complex frequencies from integral operators [29] have been studied. Also, quasinormal modes recently became quite popular [30–32]. A spectral decomposition of the T matrix can be done as well [33–35].

Among these methods, the spectral decomposition of the T matrix deals with the response on a real frequency axis. Therefore, it bypasses the necessity to project the relevant modes from the complex-frequency plane to the real-frequency axis. This seems to be preferred when linking the discussion of modes directly to observable features. Therefore, we will rely on the present work in this approach.

Many metamaterials that were shown to sustain a Fano response were fabricated with a top-down approach [36–38]. In this approach, the meta-atoms are isolated or arranged periodically in an array. The response of the entire structure can be probed with a specific incident field [39]. As the structure itself is often anisotropic, the response depends on the direction of the incident field. By tuning the parameters of the meta-atom, i.e., breaking the symmetry, and matching them with the incident field direction, strong Fano responses can be tailored [40]. This is a very deterministic process.

However, this top-down approach is not the only way to build metamaterials. As an alternative, self-assembly methods based on colloidal nanochemistry have been proposed [41–43]. In this bottom-up approach, a larger number of metallic nanoparticles are assembled into complicated meta-atoms. There are pros and cons for such an approach. Most importantly, bulk 3D materials are easily available at lower costs. The amorphous arrangement renders the optical response from such materials to be isotropic. Under the assumption of a sufficient strong dilution, the optical response from the 3D material can be derived from the ensemble-averaged properties of the isolated meta-atom. The ensemble average takes place over all possible orientations of the meta-atom relative to the illumination [44,45]. In such a situation, due to the fact that meta-atoms are randomly oriented, the definition of mode coupling becomes blurry and the concept of a Fano resonance is therefore hard to discuss.

To identify which spectral features in such ensemble averages are due to Fano resonances in the individual structure, we propose here a method to calculate the average mode cross coupling for diluted self-assembled metamaterials. This serves as the spectral signature for the Fano resonance. The quantity can be derived directly from the T matrix of the corresponding meta-atom [45]. This parameter expresses how much the coupling between the eigenmodes of the structure contributes to its total scattering cross section. This enables us to identify and discuss the previously mentioned Fano resonance also in the context of self-assembled metamaterials.

II. EXTRACTING AVERAGE MODE COUPLING FROM THE T MATRIX OF META-ATOM

Our consideration starts with the T matrix of the scatterer. The T matrix links the incident and scattered field coefficients for a given object [46]. It is an operator unique to the scatterer, independent of the illumination direction. This approach requires a decomposition of the scattered and incident fields into an orthonormal basis set to formulate the scattering problem as an algebraic one. Using such an expansion, the coefficients of scattered and incident fields can be written in a vector form and they are linked by the T matrix as

$$\overline{T}\,|p\rangle = |a\rangle\,. \tag{1}$$

Here, $|p\rangle$ and $|a\rangle$ are the vector forms of the linear coefficients from the incident and scattered fields in the chosen basis set. Throughout this paper, we will use the notation overline, such as $\overline{T}$, to describes a matrix.

To extract the modes of the meta-atom, an eigenvalue decomposition (EVD) of the T matrix is employed. The decomposition can be written as

$$\overline{T} = \overline{X}\,\overline{H}\,\overline{X}^{-1}. \tag{2}$$

In the above equation, $\overline{X}$ is a square matrix whose columns contain the eigenvectors of $\overline{T}$ and $\overline{H}$ is a diagonal matrix whose elements are the eigenvalues η_i. Here, the eigenvalue provides information on the strength of the mode, while the eigenvector describes the basis superposition of the mode [34].

As mentioned before, the usual analysis of the Fano profile of the response is often done in the context of a well-defined wave vector and polarization states of the incident field [2], as sketched in Fig. 1(a). This matches perfectly with metamaterials made from a top-down approach, where the orientation and position of each meta-atom are well defined [47]. For metamaterials made from self-assembly [42,48,49], such deterministic arrangement is lost, as meta-atoms are randomly oriented inside a solution. Usually, the response of the metamaterials made from the self-assembly approach is obtained by taking the rotationally averaged value of the response from all incident possible direction and polarization states, as shown in Fig. 1(b). It is, therefore, difficult to analyze the response of such material in general, and, in particular, to discern whether certain features originate from

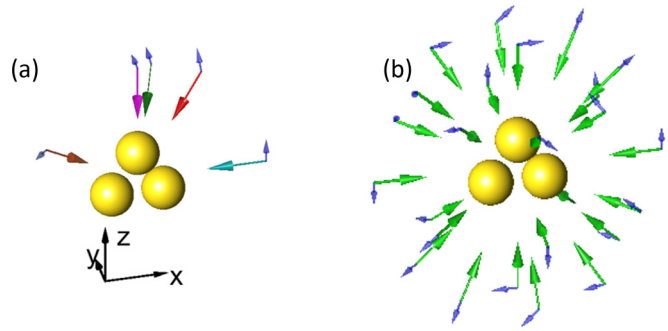

FIG. 1. (a) Illustration of different incident fields of a single trimer structure. (b) Multiple incident field scenarios to describe the response of metamaterials made from self-assembly approach. In a diluted limit, the response can be derived by taking a rotationally average value over all possible illumination and polarization directions. For each incident field, the blue semitransparent arrow denotes the electric field, and the other arrow denotes its wave vector. Please note the color of the wave vector in (a) corresponds to the color in which the optical response is shown later in the paper.

either the interaction between nonorthogonal modes or from the incoherent superposition of orthogonal modes.

To discuss the features of the response of self-assembled metamaterials, experimentally observable parameters need to be extracted directly from the T matrix of a meta-atom. It has recently been shown [45] that for a sufficiently diluted self-assembled metamaterial, the rotationally averaged properties of an individual meta-atom can be used to describe the properties of bulk self-assembled metamaterials. Here, we focus on the rotationally averaged extinction ($\sigma_{\mathrm{ext}}^{\mathrm{aver}}$), scattering ($\sigma_{\mathrm{sca}}^{\mathrm{aver}}$), and absorption ($\sigma_{\mathrm{abs}}^{\mathrm{aver}}$) cross sections of the meta-atom. They can be written as a matrix operator of the T matrix as

$$\sigma_{\mathrm{sca}}^{\mathrm{aver}} = \frac{4\pi}{k_{\mathrm{b}}^2}\mathrm{Tr}[\overline{T}^{\dagger}\,\overline{T}], \tag{3}$$

$$\sigma_{\mathrm{ext}}^{\mathrm{aver}} = \frac{4\pi}{k_{\mathrm{b}}^2}\Re\mathrm{Tr}[\overline{T}], \tag{4}$$

$$\sigma_{\mathrm{abs}}^{\mathrm{aver}} = \sigma_{\mathrm{ext}}^{\mathrm{aver}} - \sigma_{\mathrm{sca}}^{\mathrm{aver}}, \tag{5}$$

where k_{b} is the background wave number. Using EVD, these quantities can be expressed in terms of eigenmodes of the T matrix as

$$\sigma_{\mathrm{sca}}^{\mathrm{aver}} = \frac{4\pi}{k_{\mathrm{b}}^2}\mathrm{Tr}[\overline{X}^{-1\dagger}\,\overline{H}^{\dagger}\,\overline{X}^{\dagger}\,\overline{X}\,\overline{H}\,\overline{X}^{-1}], \tag{6}$$

and by applying the cyclic identity of trace. $\mathrm{Tr}[\overline{A}\,\overline{B}\,\overline{C}] = \mathrm{Tr}[\overline{B}\,\overline{C}\,\overline{A}]$,

$$\sigma_{\mathrm{sca}}^{\mathrm{aver}} = \frac{4\pi}{k_{\mathrm{b}}^2}\mathrm{Tr}[\overline{H}^{\dagger}\overline{X}^{\dagger}\overline{X}\,\overline{H}(\overline{X}^{\dagger}\overline{X})^{-1}], \tag{7}$$

and

$$\sigma_{\mathrm{ext}}^{\mathrm{aver}} = \frac{4\pi}{k_{\mathrm{b}}^2}\Re\mathrm{Tr}[\overline{H}]. \tag{8}$$

In an explicit sum, they can be written as

$$\sigma_{\mathrm{sca}}^{\mathrm{aver}} = \frac{4\pi}{k_{\mathrm{b}}^2}\sum_{\mathrm{s}=1}^{\mathrm{S}}\sum_{\mathrm{t}=1}^{\mathrm{S}}\eta_{\mathrm{s}}\eta_{\mathrm{t}}^{*}\,\langle x_{\mathrm{s}}|x_{\mathrm{t}}\rangle\,\langle y_{\mathrm{t}}|y_{\mathrm{s}}\rangle\,, \tag{9}$$

$$\sigma_{\mathrm{ext}}^{\mathrm{aver}} = \frac{4\pi}{k_{\mathrm{b}}^2}\Re\sum_{\mathrm{i}=1}^{\mathrm{S}}\eta_{\mathrm{i}}. \tag{10}$$

Here, x is the eigenvector that is obtained from the column of matrix $\overline{X}$, η is the eigenvalue, and y is the eigenvector of $T^{\dagger}$. The rotationally averaged scattering cross section can also be written as

$$\sigma_{\mathrm{sca}}^{\mathrm{aver}} = \sigma_{\mathrm{sca}}^{\mathrm{dir,aver}} + \sigma_{\mathrm{sca}}^{\mathrm{cro,aver}}, \tag{11}$$

where

$$\sigma_{\mathrm{sca}}^{\mathrm{dir,aver}} = \sum_{\mathrm{s}=1}^{\mathrm{S}}|\eta_{\mathrm{s}}|^2 \tag{12}$$

denotes the incoherent summation of all eigenmodes of the meta-atom and

$$\sigma_{\mathrm{sca}}^{\mathrm{cro,aver}} = \frac{4\pi}{k_{\mathrm{b}}^2}\sum_{\mathrm{s}=1}^{\mathrm{S}}\sum_{\mathrm{t}\neq\mathrm{s}}^{\mathrm{S}}\eta_{\mathrm{s}}\eta_{\mathrm{t}}^{*}\,\langle x_{\mathrm{s}}|x_{\mathrm{t}}\rangle\,\langle y_{\mathrm{t}}|y_{\mathrm{s}}\rangle \tag{13}$$

denotes the contribution from the cross coupling between eigenmodes. It is the contribution of the latter term that is responsible for causing the Fano features in the scattering and absorption cross sections.

To express how much the mode cross-coupling contributes to the overall scattering response from a given meta-atom, a rotationally averaged cross-coupling parameter C_{av} is introduced, defined as

$$C_{\mathrm{av}} = \frac{\sigma_{\mathrm{sca}}^{\mathrm{cro,aver}}}{\sigma_{\mathrm{sca}}^{\mathrm{aver}}}. \tag{14}$$

This equation is the most important theoretical finding of this contribution. If we study the rotationally averaged scattering cross section spectrally resolved, we can conclude that a subset of features is caused by Fano resonances if the rotationally averaged cross-coupling parameter takes large values in the same spectral domain.

The rotationally averaged extinction cross section as described in Eq. (10) is expressed only as a sum of the real part of the eigenvalues. It expresses that, on average, no mode coupling occurs when considering the rotationally averaged extinction cross section. This is in contrast to the extinction cross section for a specific incident field, where the extinction cross section can be decomposed as (the derivation can be found in the Appendix)

$$\sigma_{\mathrm{ext}} = \Re\sum_{\mathrm{i}=1}^{\mathrm{S}}\sum_{\mathrm{j}=1}^{\mathrm{S}}\eta_{\mathrm{j}}\,\langle x_{\mathrm{i}}|x_{\mathrm{j}}\rangle\,\langle y_{\mathrm{j}}|p\rangle\,\langle p|y_{\mathrm{i}}\rangle\,. \tag{15}$$

Here, the mode coupling term $\langle x_{\mathrm{i}}|x_{\mathrm{j}}\rangle$ ($\mathrm{i}\neq\mathrm{j}$), exists as long as the eigenvectors form a nonorthogonal basis set. However, all these interference terms cancel out in the averaging process. Therefore, the Fano features can only be seen in the scattering cross section, and consequently, absorption cross section as well.

For the sake of completeness, the scattering cross section for a particular incident field is [33]

$$\sigma_{\mathrm{sca}} = \frac{4\pi}{k_{\mathrm{b}}^2}\sum_{\mathrm{i}}\sum_{\mathrm{j}}\eta_{\mathrm{i}}\eta_{\mathrm{j}}^{*}\,\langle p|x_{\mathrm{j}}\rangle\,\langle y_{\mathrm{i}}|p\rangle\,\langle x_{\mathrm{i}}|x_{\mathrm{j}}\rangle\,. \tag{16}$$

Due to the fact that EVD can be done independently for each frequency, a mode tracking algorithm is needed for analyzing the modes. Here we use the mode tracking algorithm as described in Ref. [34], which fits to our problem.

III. ROTATIONALLY AVERAGED FANO FEATURES

After deriving the methodology, in this section we will apply Eq. (14) to study the Fano properties of selected meta-atoms that are correlated to the mode-coupling measure of Eq. (14) in the respective meta-atom. In this paper, we consider a meta-atom amenable for the fabrication with a bottom-up approach made from gold nanoparticles. In the simulations, the dispersion in the permittivity of gold is described by the Drude model,

$$\varepsilon_{\mathrm{Au}} = \varepsilon_{\infty} - \frac{\omega_p^2}{\omega(\omega + i\gamma)}, \tag{17}$$

where $\varepsilon_{\infty} = 9$, $\hbar\omega_p = 9$ eV, and $\hbar\gamma = 0.05$ eV [50].

Note that the choice of using a Drude model rather than experimental values is done purely for the convenience of

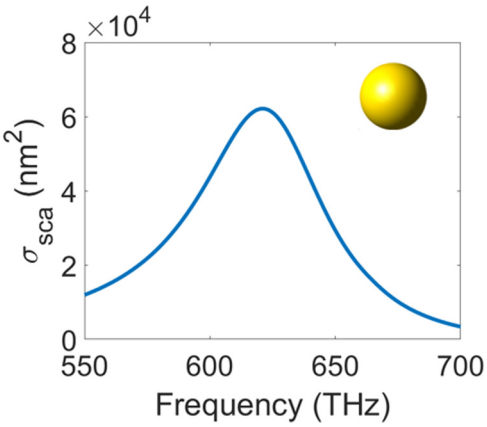

FIG. 2. Scattering cross section of a single gold nanoparticle embedded in vacuum. The radius of the gold nanoparticle is 50 nm. The permittivity of gold has been described according to Eq. (17).

providing a smooth dependency of predictable features with respect to the frequency. The scattering cross section of an individual gold nanoparticle with a radius of 50 nm as calculated with Mie theory is shown in Fig. 2. The resonance frequency happens to be around 625 THz. As the particle is isotropic, there is no dependency with respect to the direction of the incident field.

For a Fano feature to emerge, we need a system with nonorthogonal modes. For this purpose, we will consider a trimer. The choice of this meta-atom is solely based on its Fano properties for a particular incident field as already discussed in literature [14,17,35]. The radius of the gold nanoparticles which make up the trimer is again 50 nm and these particles are embedded in vacuum. The gold nanoparticles are arranged in an equilateral triangle with a center to center distance between two nanoparticles(d_t) of 120 nm, as depicted in Fig. 3.

The scattering cross section of this trimer structure for various incident plane-wave illuminations is shown in Fig. 4. The wave vector of the incident field is described by two parameters, polar angle θ and azimuthal angle ϕ. The unit vector of the wave vector, $\hat{\mathbf{k}}$, is written as $\hat{\mathbf{k}} = [k_x, k_y, k_z] = [\sin\theta\cos\phi, \sin\theta\sin\phi, \cos\theta]$. The electric field is always TM

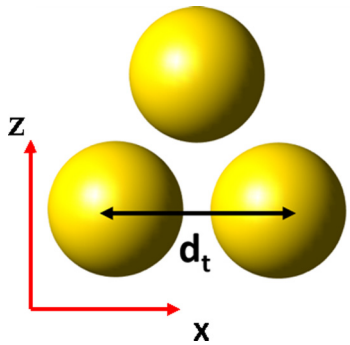

FIG. 3. The considered trimer structure made from three gold nanoparticles with a radius of 50 nm, arranged equilaterally, with the center to center distance between particle of 120 nm.

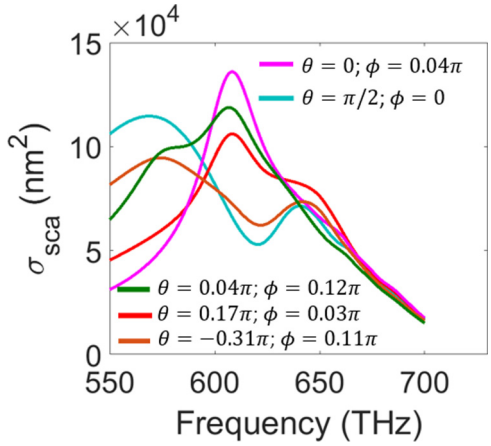

FIG. 4. Selected scattering cross section of the considered trimer structure for different illumination scenarios, denoted by the polar angle θ and azimuthal angle ϕ. Different colors denote different incident field scenarios, and correspond to the same colors as in Fig. 1(a).

mode, where the electric field is in plane between the wave vector and the z axis, as defined in Ref. [51]. The incident field has a unit amplitude and the magnetic field is chosen to assure transversality of the illumination. The different spectral behavior in the scattering cross section for different incident field scenarios is the manifestation of the spectral interference of different modes that can be excited with different strengths by the respective incident field. However, such spectral response can only be measured for a well-defined orientation between particles and illumination. In a solution that contains many such meta-atoms with a random orientation, this spectral response cannot be seen but instead the spectral average needs to be considered.

Figure 5(a) shows the rotationally averaged scattering and extinction cross sections of the structure described in Fig. 3(a). For the extinction cross section, the average is simply the sum of all modal strengths of the eigenmodes. The scattering cross section, however, can be split into the direct and the indirect contribution, as described in the figure. The rotationally averaged scattering cross section has maxima at

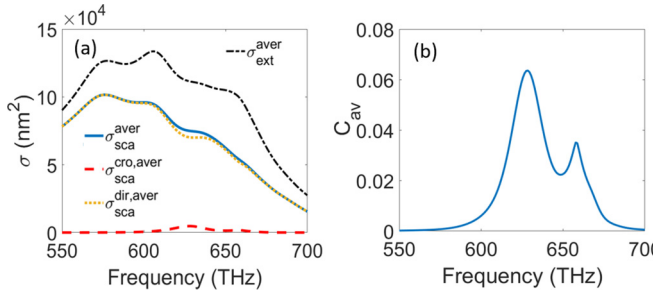

FIG. 5. (a) Rotationally averaged scattering cross section (solid blue) and its decomposition into direct (orange dotted) and cross (red dashed) terms. The extinction cross section (black dash-dotted) is also shown here. (b) Mode-coupling parameter C_{av} for the considered trimer structure.

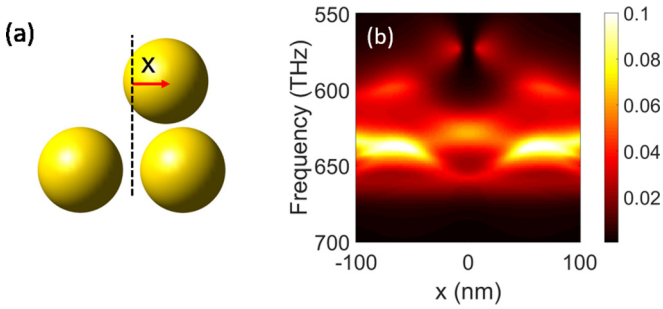

FIG. 6. (a) Symmetry breaking of trimer structure can be performed by moving the upper particle in the horizontal direction with the distance of x and (b) the corresponding contour map of the cross-coupling parameter C_{av}.

frequencies around 572, 602, and 645 THz. Note that, as previously mentioned, the maximum scattering cross section of individual gold nanoparticle occurs around 625 THz. Using this fact, it can be deduced that these peaks are the result of the coupling between nanoparticles in trimer arrangement. Indeed, it makes sense to consider them as the resonances of the supermodes of three coupled nanoparticles.

We also observe two notable dips in between these three maxima, which appear around 592 and 628 THz. By analyzing $\sigma_{\text{sca}}^{\text{cro,aver}}$, we can conclude that the dip at 592 THz appears due to the incoherent summation of the modes of the structure, as the value of $\sigma_{\text{sca}}^{\text{cro,aver}}$ is negligible. In contrast, the dip at 628 THz is the result of mode coupling in the structure. At this frequency, the value of $\sigma_{\text{sca}}^{\text{cro,aver}}$ reaches its maximum. This can be seen in much more detail from the cross-coupling parameter as shown in Fig. 5(b). Here, the cross-coupling parameter, C_{av}, happens to have two peaks, one around 628 THz and the other one around 659 THz.

By comparing the results from Figs. 3(b) and 5(a), it can be seen that only the dip around 630 THz and small dip around 652 THz for various incident angles, and notably for $\theta = \frac{\pi}{2}; \psi = 0$, correspond to mode cross coupling, which happen when the corresponding nonorthogonal modes get excited. They are caused from Fano resonances of the individual structure.

IV. EFFECT OF THE SYMMETRY OF META-ATOMS

Symmetry plays an important role in the Fano response. It was shown that by breaking the symmetry of the system, a more pronounced Fano effect can be observed [14,40,52]. For this particular reason, we will study in this section the effect of the symmetry of the meta-atom on the cross-coupling parameter. For this purpose, we will focus our case study to the trimer structure as described in the previous section, since it provides a rather simple geometry to be analyzed. Here, we break the symmetry of the structure by shifting the upper particle.

Figure 6(a) shows breaking of symmetry by moving the upper particle in the x direction. This will break both rotational and mirror symmetry of the structure. The effect of this symmetry breaking to mode cross coupling, C_{av}, for various displacements of the upper sphere of the trimer along the x direction can be seen in Fig. 6(b). The maximum value of C_{av} appears at frequencies around 630 THz and x around 60 nm. It can be attributed to a strong coupling between the upper sphere and the sphere below it. At this distance of 60 nm, the upper sphere is exactly above one of the lower spheres, meaning that the distance between them is at its minimum. This phenomena can also be understood if we analyze the problem from eigenmodes of the subsystem. Here, the mode from the upper sphere can be considered as a bright mode, and the modes excited in the two lower spheres can be considered as dark. For a minimum distance, the coupling between two spheres in the structure is maximal. Hence, it is no surprise that the mode coupling of the structure increases.

To understand the origin of the increases of mode cross coupling due to the breaking of symmetry, we will compare the modal strength of a perfect trimer ($x = 0$ nm) with the case of one sphere completely above another sphere ($x =$ 60 nm). Figure 7(a) shows the modal strengths for 11 dominant eigenmodes and their corresponding multipolar compositions for the unperturbed trimer structure. Here, we choose these 11 eigenmodes with the much larger modal strengths (>50 times) compared to that of other eigenmodes. These other eigenmodes with very small modal strength are not shown here for the sake of clarity. Note that the T-matrix description in Eq. (1) is valid for any orthonormal basis set, and our C_{av} is a basis-independent parameter.

To perform a more detailed analysis, we now choose a particular basis: the multipolar fields as defined in Ref. [53] in the following discussion. With such a basis set, the scattered $\mathbf{E}_{\text{sca}}(\mathbf{r}, \omega)$ and incident $\mathbf{E}_{\text{inc}}(\mathbf{r}, \omega)$ fields can be decomposed as

$$\mathbf{E}_{\text{sca}}(\mathbf{r}, \omega) = \sum_{k=1}^{2} \sum_{\text{n}=1}^{\text{N}} \sum_{\text{m}=-\text{n}}^{\text{n}} a_{\text{nmk}} \mathbf{M}_{\text{nmk}}^{(3)}(\mathbf{r}, \omega), \tag{18}$$

$$\mathbf{E}_{\text{inc}}(\mathbf{r}, \omega) = \sum_{\text{k}=1}^{2} \sum_{\text{n}=1}^{\text{N}} \sum_{\text{m}=-\text{n}}^{\text{n}} p_{\text{nmk}} \mathbf{M}_{\text{nmk}}^{(1)}(\mathbf{r}, \omega), \tag{19}$$

where $\mathbf{M}_{\text{nmk}}^{(i)}(\mathbf{r})$ refers to the vector spherical wave functions, p_{nmk} and a_{nmk} are the expansion coefficients, index k refers to the parity of the vector spherical harmonics, n and m are integer numbers, and N describes the maximum multipolar order taken into account. The superscript denotes the radial function of the vector spherical harmonics. Superscript 1 means spherical Bessel function of the first kind and superscript 3 means spherical outgoing Hankel function.

By using vector spherical harmonics as our basis set, we can argue that mode coupling occurs because different modes share the same multipolar contributions. To quantify these

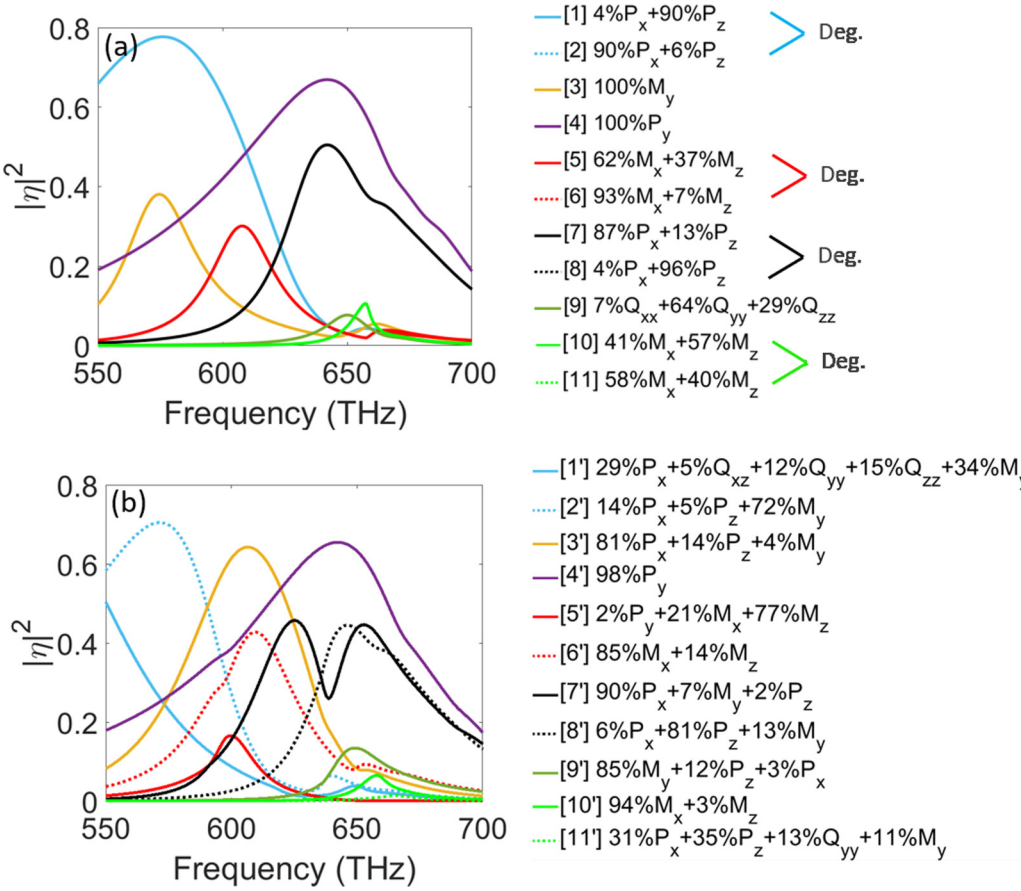

FIG. 7. Modal strength and its multipolar components of 11 dominant eigenmodes of (a) a perfect trimer structure. Here, four of them are degenerate modes as pointed out by the same color and additional grouping denoted by Deg. In the case of modes 10 and 11, we multiply their modal strength by a factor of 10 for visibility. (b) Modal strength and its multipolar components of 11 dominant eigenmodes for the asymmetric trimer when $x = 60$ nm. The same multiplication by a factor of 10 is also done here for modes 10′ and 11′. Here, the upper sphere is directly on top of one of the spheres on the bottom. P, M, and Q denote electric dipole, magnetic dipole, electric quadrupole, while the subscript denotes its component. Here, the multipolar decomposition of each eigenmode is analyzed at a frequency 637 THz.

multipolar contributions, we define the multipole moments as

$$\begin{pmatrix} P_x \\ P_y \\ P_z \end{pmatrix} = \begin{pmatrix} (a_{1,1,1} - a_{1,-1,1}) \\ i(a_{1,1,1} + a_{1,-1,1}) \\ -\sqrt{2}a_{1,0,1} \end{pmatrix}, \tag{20}$$

$$\begin{pmatrix} M_x \\ M_y \\ M_z \end{pmatrix} = \begin{pmatrix} (a_{1,1,2} - a_{1,-1,2}) \\ i(a_{1,1,2} + a_{1,-1,2}) \\ -\sqrt{2}a_{1,0,2} \end{pmatrix}, \tag{21}$$

$$\begin{pmatrix} Q_{xx} & Q_{xy} & Q_{xz} \\ Q_{yx} & Q_{yy} & Q_{yz} \\ Q_{zx} & Q_{zy} & Q_{zz} \end{pmatrix} = \frac{1}{6\sqrt{5}} \begin{pmatrix} i(a_{2,2,1} + a_{2,-2,1}) - \frac{i\sqrt{6}}{2}a_{2,0,1} & (a_{2,-2,1} - a_{2,2,1}) & i(a_{2,-1,1} - a_{2,1,1}) \\ (a_{2,-2,1} - a_{2,2,1}) & -i(a_{2,2,1} + a_{2,-2,1}) - \frac{i\sqrt{6}}{2}a_{2,0,1} & (a_{2,-1,1} + a_{2,1,1}) \\ i(a_{2,-1,1} - a_{2,1,1}) & (a_{2,-1,1} + a_{2,1,1}) & i\sqrt{6}a_{2,0,1} \end{pmatrix}, \tag{22}$$

where P, M, and Q denote electric dipole, magnetic dipole, and electric quadrupole moments, respectively, and the spherical multipole coefficients a_{nmk} are taken from the eigenmodes of the T matrix. The subscript in the above equations denotes its components in the Cartesian basis set. Possible further prefactors are neglected, since we are more interested in the fraction of each multipolar component relative to the total sum of all multipoles, that is $|P_x|^2 + |P_y|^2 + \cdots + |Q_{zz}|^2 = 100\%$.

By analyzing the multipolar contributions from each eigenmode, the analysis of the origin of mode coupling can be done in a more convenient way, as shown in Fig. 7. In particular and besides the modal strength in the actual figure, the figure legend indicates the fraction of the different multipolar

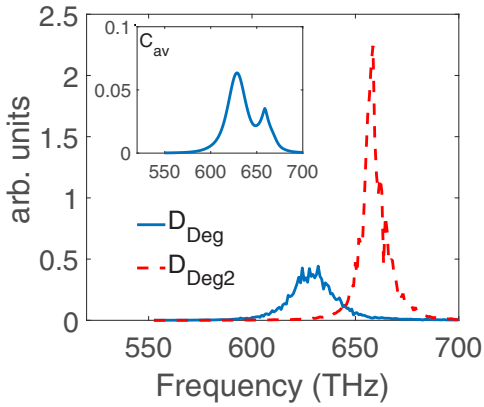

FIG. 8. Mode nonorthogonality between modes, D_{Deg} and D_{Deg2}. Here, they are defined as $D_{\mathrm{deg}} = (D_{17} + D_{27} + D_{18} + D_{28})$ and $D_{\mathrm{deg2}} = (D_{5,10} + D_{6,10} + D_{5,11} + D_{6,11})$. Here, the peaks of mode nonorthogonality correspond to the observed peaks of C_{av}. The inset shows mode cross-coupling parameter, C_{av} for perfect trimer structure ($x = 0$ nm).

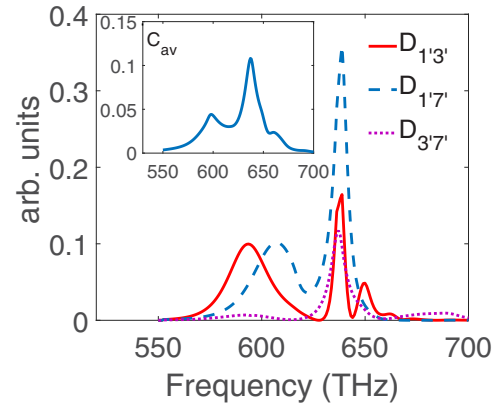

FIG. 9. Mode nonorthotgonality of selected modes described in Fig. 7(b). Here, the mode nonorthogonality is defined according to Eq. (23), while the subscript denotes the modes described in Fig. 7(b). The inset shows mode cross-coupling parameter, C_{av} for $x = 60$ nm.

contributions to the respective eigenmode. Here, we neglect the multipolar contributions which are lower than 2%. Please note, modes 1 and 2 are degenerate for the high-symmetry structure, i.e., for no displacement of the particle. The same applies to modes 5 and 6, modes 7 and 8, and modes 10 and 11. They are plotted in Fig. 7 in the same color but with either a dashed or a solid line. The curves for degenerate modes in Fig. 7(a) are therefore not distinguishable. This is because they are on top of each other. Special care needs to be taken for modes 10 and 11, as their modal strength is relatively small. In Fig. 7, we multiply their modal strength by a factor of 10. The degeneracy is broken in Fig. 7(b). From the figure, and particularly its legend, it can be seen that the modes indicated by the cyan (modes 1 and 2) and black (modes 7 and 8) lines in Fig. 7(a) share P_x and P_z components. This results in nonorthogonality between these modes. By breaking the symmetry of the structure, in this case, by moving the upper particle such that it is above one of the other spheres, the modal strengths as well as its multipolar compositions undergo a change, but they remain nonorthogonal. Note that for the mode plotted in purple (mode 4), the modal strength and its multipolar composition almost undergo no change. This can be understood as this particular mode is dominated by a y-polarized electric dipole moment, being only weakly affected by a change of the particle position in the x-z plane. On the other hand, different eigenmodes with mixed multipolar composition appear naturally due to the breaking of symmetry, as shown in Fig. 7(b). Since most of them share the same multipolar moments, this will result in the increase of mode cross coupling, as was observed in Fig. 6(a).

To develop further the argument described before, Fig. 8 shows the mode nonorthogonality of selected modes described in Fig. 7(a). Here, we define the mode nonorthogonality between mode i and j, D_{ij} as

$$D_{\mathrm{ij}} = \frac{|\langle x_{\mathrm{i}}|x_{\mathrm{j}}\rangle|^2}{\langle x_{\mathrm{i}}|x_{\mathrm{i}}\rangle\,\langle x_{\mathrm{j}}|x_{\mathrm{j}}\rangle}, \tag{23}$$

where the subscript denotes the mode index as shown in Fig. 7. Here, we are dealing with the degenerate modes. Due to this reason, we define the mode nonorthogonality D_{deg} as the sum of the mode nonorthogonality between all the modes; that is, $D_{\mathrm{deg}} = (D_{17} + D_{27} + D_{18} + D_{28})$. The same definition applies for D_{deg2}, where it is the sum of the mode nonorthogonality between modes 5 and 6 and modes 10 and 11. Here, we can see that the peaks observed in Fig. 5(b) match quite perfectly with the peaks observed here. The peak around 630 THz is due to the coupling between modes 1 and 2 and modes 7 and 8, while the peak around 660 THz is the result of the coupling between modes 5 and 6 and modes 10 and 11. Due to the fact that the cross-coupling term in the definition of C_{av} [see Eq. (13)] contains the eigenvalue terms, this is the reason that the amplitudes of mode nonorthogonality presented in Fig. 8 are not the same as the amplitude of it's corresponding C_{av}. Nevertheless, the origin of these two peaks in C_{av} can be tracked to the nonorthogonality between modes involved.

By using the same analysis, the mode nonorthogonality between different modes for the case of $x = 60$ nm can also be obtained, as shown in Fig. 9. Here, the primed subscripts refer to the modes of the structure with one particle being displaced [Fig. 7(b)]. When plotting the mode nonorthogonality of selected modes, the inset here shows the corresponding C_{av}. Here, we can conclude that the peak that appears around 600 THz is mainly due to the coupling between modes $1'$ and $3'$ and also modes $1'$ and $7'$. On the other hand, the dominant peak around 640 THz is due to the contribution of coupling between these three modes.

V. CONCLUSIONS

In this paper, we introduce a parameter to quantify the rotationally averaged mode cross coupling of a meta-atom. The parameter can be used to quantify the Fano response of self-assembled metamaterials of the bulk system made from this meta-atom. The analysis shows that the rotationally averaged mode coupling in the extinction cross section is always

zero, meaning the interaction between modes are canceling each other while taking the average. On the other hand, mode coupling plays an important role in the description of the scattering cross section. Here, the response can be decomposed into the contribution resulting from the interaction between modes and the direct contribution from each mode. By analyzing the cross-coupling parameter introduced in this paper, it is shown that by breaking the symmetry of the system, a higher cross-coupling measure can be achieved. Here, we show that the origin of the spectral behavior of $C_{\rm av}$ is due to coupling between different modes which share the same multipolar components. With this, we provide a way to analyze Fano resonances in self-assembled metamaterials. This paper may provide impetus for designing isotropic metamaterials with Fano properties.

ACKNOWLEDGMENTS

This work was supported by the Deutsche Forschungsgemeinschaft/ German Science Foundation (Project No. RO 3640/4-1). R.N.S.S. also acknowledges support from Karlsruhe School of Optics & Photonics (KSOP). R.N.S.S. also acknowledges travel support from Karlsruhe House of Young Scientists through International Collaboration package grant. R.N.S.S. would like to thank Andreas Vetter for proofreading the paper.

APPENDIX: MODAL DECOMPOSITION OF EXTINCTION CROSS SECTION

The extinction cross section of a scatterer can be calculated from the expansion coefficients of the scattered and incident fields. The expression of such a quantity is

$$\sigma_{\rm ext} = \frac{4\pi}{k_{\rm b}^2} \Re \langle p|a\rangle \,, \tag{A1}$$

where $\sigma_{\rm ext}$ and $k_{\rm b}$ denote the extinction cross section and wave number in the background medium, while $|p\rangle$ and $|a\rangle$ denote the vector column whose entries are the linear coefficients of the incident and scattered fields, respectively. By expanding the incident field in terms of eigenvectors of the T matrix and using the biorthogonality relation [54],

$$|p\rangle = \sum_{\rm i=1}^{\rm S} |x_{\rm i}\rangle \langle y_{\rm i}| \, |p\rangle = \sum_{\rm i=1}^{\rm S} \langle y_{\rm i}|p\rangle \, |x_{\rm i}\rangle \,, \tag{A2}$$

$$|a\rangle = \overline{T} \, |p\rangle = \overline{T} \sum_{\rm i=1}^{\rm S} \langle y_{\rm i}|p\rangle \, |x_{\rm i}\rangle \,. \tag{A3}$$

Using the fact that

$$\overline{T} \, |x_{\rm i}\rangle = \eta_{\rm i} \, |x_{\rm i}\rangle \,, \tag{A4}$$

the scattered field coefficients can be written as

$$|a\rangle = \sum_{i=1}^{\rm S} \langle y_{\rm i}|p\rangle \, \eta_{\rm i} \, |x_{\rm i}\rangle \,, \tag{A5}$$

and the decomposition of extinction cross section into eigenmodes of the structure is

$$\sigma_{\rm ext} = \frac{4\pi}{k_{\rm b}^2} \Re \sum_{\rm i=1}^{\rm S} \sum_{\rm j=1}^{\rm S} \eta_{\rm j} \langle x_{\rm i}|x_{\rm j}\rangle \langle y_{\rm j}|p\rangle \langle p|y_{\rm i}\rangle \,. \tag{A6}$$

[1] B. Luk'yanchuk, N. I. Zheludev, S. A. Maier, N. J. Halas, P. Nordlander, H. Giessen, and C. T. Chong, Nat. Mater. **9**, 707 (2010).
[2] M. F. Limonov, M. V. Rybin, A. N. Poddubny, and Y. S. Kivshar, Nat. Photon. **11**, 543 (2017).
[3] B. Luk'yanchuk, A. Miroshnichenko, and Y. S. Kivshar, J. Opt. **15**, 073001 (2013).
[4] Y. Liu and X. Zhang, Chem. Soc. Rev. **40**, 2494 (2011).
[5] W.-S. Chang, J. B. Lassiter, P. Swanglap, H. Sobhani, S. Khatua, P. Nordlander, N. J. Halas, and S. Link, Nano Lett. **12**, 4977 (2012).
[6] J. Zhao, C. Zhang, P. V. Braun, and H. Giessen, Adv. Mater. **24**, OP247 (2012).
[7] T. Wu, Y. Liu, Z. Yu, H. Ye, C. Shu, Y. Peng, J. Wang, and H. He, Mod. Phys. Lett. B **29**, 1550218 (2015).
[8] J. Ye, F. Wen, H. Sobhani, J. B. Lassiter, P. Van Dorpe, P. Nordlander, and N. J. Halas, Nano Lett. **12**, 1660 (2012).
[9] Z. Zhu, B. Bai, O. You, Q. Li, and S. Fan, Light: Sci. Appl. **4**, e296 (2015).
[10] Y. Yang, W. Wang, A. Boulesbaa, I. I. Kravchenko, D. P. Briggs, A. Puretzky, D. Geohegan, and J. Valentine, Nano Lett. **15**, 7388 (2015).
[11] K. Thyagarajan, J. Butet, and O. J. Martin, Nano Lett. **13**, 1847 (2013).
[12] L. Hu, Y. Huang, L. Fang, G. Chen, H. Wei, and Y. Fang, Sci. Rep. **5**, 16069 (2015).
[13] B. Hopkins, A. N. Poddubny, A. Miroshnichenko, and Y. S. Kivshar, Laser Photonics Rev. **10**, 137 (2016).
[14] B. Gallinet and O. J. F. Martin, ACS Nano **5**, 8999 (2011).
[15] B. Gallinet and O. J. F. Martin, Phys. Rev. B **83**, 235427 (2011).
[16] V. Flauraud, G. D. Bernasconi, J. Butet, M. Mastrangeli, D. T. Alexander, O. J. Martin, and J. Brugger, ACS Photonics **4**, 1661 (2017).
[17] B. Hopkins, A. N. Poddubny, A. E. Miroshnichenko, and Y. S. Kivshar, Phys. Rev. A **88**, 053819 (2013).
[18] B. Hopkins, D. S. Filonov, A. E. Miroshnichenko, F. Monticone, A. Alü, and Y. S. Kivshar, ACS Photonics **2**, 724 (2015).
[19] B. Hopkins, D. S. Filonov, S. B. Glybovski, and A. E. Miroshnichenko, Phys. Rev. B **92**, 045433 (2015).
[20] J. Mäkitalo, M. Kauranen, and S. Suuriniemi, Phys. Rev. B **89**, 165429 (2014).
[21] C. E. Baum, DTIC Document (1971), http://www.dtic.mil/docs/citations/ADA066905.
[22] D. J. Riley, W. A. Davis, and I. M. Besieris, Radio Sci. **20**, 20 (1985).
[23] R. Garbacz and R. Turpin, IEEE Trans. Antennas. Propag. **19**, 348 (1971).

[24] M. Cabedo-Fabres, E. Antonino-Daviu, A. Valero-Nogueira, and M. F. Bataller, IEEE Antennas Propag. Mag. **49**, 52 (2007).
[25] D. J. Bergman and D. Stroud, Phys. Rev. B **22**, 3527 (1980).
[26] X. Zheng, V. Volskiy, V. K. Valev, G. A. E. Vandenbosch, and V. V. Moshchalkov, IEEE J. Sel. Top. Quantum Electron. **19**, 4600908 (2013).
[27] N. A. Gippius, T. Weiss, S. G. Tikhodeev, and H. Giessen, Opt. Express **18**, 7569 (2010).
[28] D. A. Bykov and L. L. Doskolovich, J. Lightwave Technol. **31**, 793 (2013).
[29] D. A. Powell, Phys. Rev. B **90**, 075108 (2014).
[30] C. Sauvan, J. P. Hugonin, I. S. Maksymov, and P. Lalanne, Phys. Rev. Lett. **110**, 237401 (2013).
[31] P. Lalanne, W. Yan, K. Vynck, C. Sauvan, and J.-P. Hugonin, Laser Photonics Rev. **12**, 1700113 (2018).
[32] W. Yan, R. Faggiani, and P. Lalanne, Phys. Rev. B **97**, 205422 (2018).
[33] M. S. Khajeahsani, A. Shahmansouri, M. J. Armand, and B. Rashidian, J. Opt. Soc. Am. B **32**, 2333 (2015).
[34] R. N. S. Suryadharma, M. Fruhnert, I. Fernandez-Corbaton, and C. Rockstuhl, Phys. Rev. B **96**, 045406 (2017).
[35] R. N. S. Suryadharma, M. Fruhnert, C. Rockstuhl, and I. Fernandez-Corbaton, Phys. Rev. A **95**, 053834 (2017).
[36] L. Chen, J. Gao, W. Xia, S. Zhang, S. Tang, W. Zhang, D. Li, X. Wu, and Y. Du, Phys. Rev. B **93**, 214411 (2016).
[37] J. B. Lassiter, H. Sobhani, J. A. Fan, J. Kundu, F. Capasso, P. Nordlander, and N. J. Halas, Nano Lett. **10**, 3184 (2010).
[38] D. Dregely, M. Hentschel, and H. Giessen, ACS Nano **5**, 8202 (2011).
[39] Y. Moritake and T. Tanaka, Sci. Rep. **8**, 9012 (2018).
[40] R. Singh, I. A. Al-Naib, M. Koch, and W. Zhang, Opt. Express **19**, 6312 (2011).
[41] Z. Nie, A. Petukhova, and E. Kumacheva, Nat. Nanotech. **5**, 15 (2010).
[42] D. A. Pawlak, S. Turczynski, M. Gajc, K. Kolodziejak, R. Diduszko, K. Rozniatowski, J. Smalc, and I. Vendik, Adv. Funct. Mater. **20**, 1116 (2010).
[43] T. Bürgi, Nanoscale **7**, 15553 (2015).
[44] Z. Fan and A. O. Govorov, Nano Lett. **10**, 2580 (2010).
[45] R. N. Suryadharma and C. Rockstuhl, Materials **11**, 213 (2018).
[46] P. C. Waterman, Proc. IEEE **53**, 805 (1965).
[47] Y. Cao, Y. Wang, Z. Geng, J. Liu, Y. Yang, and H. Chen, J. Appl. Phys. **117**, 063107 (2015).
[48] V. Ponsinet, A. Baron, E. Pouget, Y. Okazaki, R. Oda, and P. Barois, Europhys. Lett. **119**, 14004 (2017).
[49] B. Gong, X. Zhao, Z. Pan, S. Li, X. Wang, Y. Zhao, and C. Luo, Sci. Rep. **4**, 4713 (2014).
[50] V. Myroshnychenko, J. Rodríguez-Fernández, I. Pastoriza-Santos, A. M. Funston, C. Novo, P. Mulvaney, L. M. Liz-Marzan, and F. J. G. de Abajo, Chem. Soc. Rev. **37**, 1792 (2008).
[51] Y.-L. Xu, Appl. Opt. **34**, 4573 (1995).
[52] S. Dutta-Gupta and O. J. Martin, J. Opt. Soc. Am. B **32**, 194 (2015).
[53] R. Alaee, C. Rockstuhl, and I. Fernandez-Corbaton, Adv. Opt. Mater. **7**, 1800783 (2019).
[54] C. Brezinski, *Biorthogonality and Its Applications to Numerical Snalysis* (CRC Press, New York, 1991), Vol. 156.